FRONT MATTER

Unconventional interlayer exchange coupling via chiral phonons in synthetic magnetic oxide heterostructures

Authors

Seung Gyo Jeong[1], Jiwoong Kim[2], Ambrose Seo[3], Sungkyun Park[2], Hu Young Jeong[4], Young-Min Kim[5], Valeria Lauter[6], Takeshi Egami[7,8], Jung Hoon Han[1], and Woo Seok Choi[1,*].

Affiliations

[1]Department of Physics, Sungkyunkwan University, Suwon 16419, Korea
[2]Department of Physics, Pusan National University, Busan 46241, Korea
[3]Department of Physics and Astronomy, University of Kentucky, Lexington, KY 40506, USA
[4]UNIST Central Research Facilities and School of Materials Science and Engineering, Ulsan National Institute of Science and Technology, Ulsan 44919, Korea
[5]Department of Energy Sciences, Sungkyunkwan University, Suwon 16419, Korea
[6]Neutron Scattering Division, Oak Ridge National Laboratory, Oak Ridge, TN 37831, USA
[7]Materials Science and Technology Division, Oak Ridge National Laboratory, Oak Ridge, TN 37831, USA
[8]Department of Materials Science and Engineering, University of Tennessee, Knoxville, TN 37996, USA
*Corresponding author. Email: choiws@skku.edu

Abstract

Chiral symmetry breaking of phonons plays an essential role in emergent quantum phenomena owing to its strong coupling to spin degree of freedom. However, direct experimental evidence of the chiral phonon-spin coupling is lacking. In this study, we report a chiral phonon-mediated interlayer exchange interaction in atomically controlled ferromagnetic metal ($SrRuO_3$)-nonmagnetic insulator ($SrTiO_3$) heterostructures. Owing to the unconventional interlayer exchange interaction, we have observed rotation of magnetic moments as a function of nonmagnetic insulating spacer thickness, resulting in a novel spin spiral state. The chiral phonon-spin coupling is further confirmed by phonon Zeeman effects. The existence of the chiral phonons and their interplay with spins along with our atomic-scale heterostructure approach open a window to unveil the crucial roles of chiral phonons in magnetic materials.

Teaser

Chiral phonons and their strong coupling with spins manifest unconventional interlayer exchange interaction and resultant novel spin state.

MAIN TEXT

Introduction

Chiral phonon serves as a fundamental element in realizing non-trivial quantum mechanical phenomena. When chiral symmetry breaks in a crystal, chiral phonons emerge and can couple to spins leading to phenomena such as phonon Hall effect, optically driven effective magnetic field, AC Stark effect, topologically-induced viscosity split, and pseudogap phase, as summarized in Table 1 (*1-16*). So far, thermal Hall and time-resolved spectroscopic measurements were employed for identifying the signatures of chiral phonons (*6-8*). However, a static manifestation of chiral phonons determining a ground state with long-range spin ordering is lacking.

Synthetic magnetic heterostructures let us study an interlayer exchange coupling (IEC), which might originate from the chiral phonon-spin coupling, e.g., the spin polarization of hole carriers by elliptically polarized phonons (*2*). In general, when two ferromagnetic (FM) layers are separated by a thin nonmagnetic-*metallic* (NM-*M*) spacer, the relative spin orientation of the FM layers is determined by the well-known Ruderman-Kittel-Kasuya-Yosida (RKKY) interaction via itinerant electrons (Fig. 1A). Here, the interlayer exchange constant (J) between the localized spins in the FM layers oscillates as a function of the spacer layer thickness (t) with the term $\cos(2k_F t) / t^d$, where k_F and d are the Fermi wavevector of the itinerant electrons in the spacer and the dimensionality of the system, respectively (*17, 18*). Hence, both parallel and antiparallel spin ordering between the FM layers can be realized depending on t, where the antiparallel alignment is commonly referred to as synthetic antiferromagnetic (sAFM) ordering. In contrast, for a nonmagnetic-*insulating* (NM-*I*) spacer without any itinerant carriers, J is known to decay monotonically and exponentially with t, above the quantum tunneling thickness regime (*18, 19*). In the presence of chiral phonons, however, we propose that spins in the FM layers can indirectly interact with each other through a NM-I spacer via chiral phonon-spin coupling. Furthermore, depending on t, the interaction effectively changes the relative spin orientations of each FM layer (Figs. 1B and 1C).

We employed atomically designed $SrRuO_3/SrTiO_3$ (SRO/STO) superlattices to model the FM-M / NM-I / FM-M heterostructure. FM SRO (FM-M layer) is an excellent candidate for the realization of unconventional IEC, owing to its strong spin-phonon and spin-orbit coupling (*20-22*). A small Fermi energy mismatch between SRO and STO (NM-I layer) and their non-polar nature highly suppresses the charge transfer across the interface (*23-25*). Furthermore, identical *A*-site ion (*i.e.*, Sr) and similar in-plane lattice constants between SRO and STO provide coherent superlattice structures with fully strained states, *i.e.*, without misfit dislocations, of which the configuration amplifies the experimental signal (*21, 24*). In particular, the ferromagnetic molecular field of SRO layers breaks the degeneracy, enabling disparate population of the chiral phonons. The structural similarity of the perovskites and atomically sharp interfaces further facilitate the chiral phonon propagation, allowing chiral phonon-spin interaction in the neighboring SRO layers.

We deliberately grew oxide superlattices with alternating α and β atomic unit cells (~0.4 nm) of SRO (t_{SRO}) and STO (t_{STO}), respectively, repeated for γ times on STO (001) substrates, *i.e.*, $[\alpha|\beta]_\gamma$, using pulsed laser epitaxy (See methods and Figs. S1-S3) (*21, 24-27*). An intriguing oscillation in the in-plane magnetization is observed as a function of t_{STO}, indicating the presence of an unconventional IEC across the NM-I spacer. The non-collinear spiral spin state in the ground state responsible for the observed magnetic oscillation was visualized by polarized neutron reflectometry (PNR). We propose chiral phonon-spin coupling as a possible mechanism for the unconventional IEC across the NM-I spacer. In particular, we suggest that the angular momentum of the chiral phonons couple to the spins, leading to the spin spiral state in our superlattices. Strong spin-phonon coupling was indeed evidenced by confocal Raman spectroscopy. This new type of long-range magnetic interaction yields an advanced understanding of the chiral phonons and accessible controllability of spiral spin states over them via atomic-scale heterostructuring. The spatial modulation of in-plane magnetization might further provide insight into the emergence of exotic spin orderings such as magnetic cone or fan (*28, 29*).

Results

NM-I thickness-dependent oscillatory magnetization behavior

The SRO/STO superlattices exhibit an exotic in-plane magnetic behavior that has not been observed in single SRO films (Figs. 1D-1G and Fig. S4). Temperature- (*T*-) dependent magnetization (M (T)) curves of the $[6|\beta]_{10}$ superlattices along the in-plane direction, for example, commonly reveal a typical FM T_c = ~130 K, followed by an anomalous Néel-like downturn at ~80 K (Fig. 1D). Note that the out-of-plane M (T) shows the conventional FM behaviors of SRO with the same T_c and without any downturn, consistent with previous studies (Fig. S5) (*21, 24-27*). Magnetic field- (*H*-) dependent in-plane magnetization (M (H)) curves of the superlattices consistently support the AFM-like behavior, with a double hysteresis loop and a large coercive field of ~1.8 T appearing below 80 K (Figs. 1E and 1F, Fig. S6). Furthermore, *H*-dependent M (T) curves show a gradual disappearance of the downturn as H is increased, especially above coercive field (Fig. S6). Similar behavior was reported in low-dimensional materials and understood as the AFM-like IEC between the FM layers (*19, 30*).

A clear t_{STO}-dependent oscillation of in-plane magnetization was observed, demonstrating the presence of unconventional IEC. We extracted M (2 K, 0.01 T) values as a function of both t_{SRO} and t_{STO}, which exhibit a distinct oscillation as a function of t_{STO} when $t_{SRO} \geq$ 1.6 nm (Fig. 1G). Note that the oscillation of the net magnetization was directly picked up from the magnetization value. This underscores the intrinsic nature of the oscillation in our superlattices, distinguishing it from the oscillations observed in the exchange bias reported by other studies (*31-34*). For example, SRO/NM-M/SRO heterostructure has shown exchange bias possibly originating from the RKKY interaction (*35*), yet M (H) curves of the SRO/STO superlattices do not show any exchange bias. Superlattices with t_{SRO} = 0.8 nm or less show negligible in-plane M (T) possibly owing to the reduced dimensionality (*24*). But M (2 K) of superlattices with sub-atomic unit cells t_{STO} control also presents a portion of the magnetic oscillation (Fig. S7). Fig. 1F further shows that the M (H) curve for the superlattices with thick STO layer (*i.e.*, $[6|18]_{10}$ superlattice, t_{STO} = ~7 nm) returns to conventional single FM hysteresis loop with nearly the same saturation magnetization to the $[6|6]_{10}$ superlattice. The downturn of M (T) with decreasing T also disappears for the $[6|18]_{10}$ superlattice. These results indicate that an unconventional IEC plays a key role in the exotic AFM-like magnetic ground state of the superlattices with thin STO layers.

We fabricated more than 350 superlattices and measured the in-plane magnetization for more than 40 of those samples and achieved excellent reproducibility in both structural and magnetic properties (Fig. S8). This confirms that the t_{STO}-dependent oscillation of the net magnetization in the superlattices is intrinsic, and does not originate from short-range ordering mechanisms such as spin-glass behavior. We note that the out-of-plane magnetization of the superlattices serves as the magnetic easy axis identical to the single SRO film (Figs. S4 and S5), but does not exhibit the peculiar oscillatory behavior. The oscillation is observed only for the relatively small, in-plane magnetization, demonstrating a stronger susceptibility to the unconventional IEC. The small in-plane magnetization further complicates the application of conventional IEC analyses using the M (H) curves. Thus, to characterize the magnetic ground states of the superlattices, we focused on the in-plane magnetic behavior and spin structures at low-H fields below 80 K.

Synthetic spiral spin state

The depth profile of the spin vector orientation along the in-plane direction of each FM layer supports the IEC-induced spiral spin ordering (Fig. 2), and resultant STO-thickness dependent oscillation of the net magnetization. Fig. 2A shows the PNR spectra of the $[6|4]_{10}$ superlattice measured at 5 K with 0.01 T in-plane H-field. R^+ (R^-) corresponds to the reflectivity measured with neutron spin parallel (antiparallel) to H. The superlattice peak at $Q = \sim 1.6\ nm^{-1}$ corresponds to the periodicity of the superlattice structures, consistent with the layer thicknesses obtained using X-ray reflectivity and scanning tunneling electron microscopy (Figs. S2, S3, and Table S1). Spin asymmetry (S. A. = $(R^+ - R^-)/(R^+ + R^-)$) exhibits a distinct structure at $Q = \sim 0.8\ nm^{-1}$ (half of the superlattice peak Q value), indicating the existence of AFM ordering (Fig. 2B) (*19, 36, 37*). (We focused on the result of $[6|4]_{10}$ superlattice as the peak values at $Q = \sim 0.8$ and $\sim 1.6\ nm^{-1}$ provided the largest signal to noise ratio. We also did not carry out the spin-flip polarization because the PNR signals were estimated to be quite small (Fig. S9) (*36*).) To characterize the synthetic spin structure of the superlattice, we assumed that each FM SRO layer has a single spin orientation with an identical total magnetization, and the spin orientation of a neighboring layer has a relative angle difference of ϕ, depending on t_{STO} (Supplementary Text 1). The β- and γ- dependent M (2 K) were fit to result in $\phi = \sim 160^{o}$ between the FM layers for $t_{STO} = 1.6$ nm, indicating a non-collinear spiral spin structure (Fig. S10). Fig. 2E visualizes the constructed spiral spin structure along the in-plane direction of the superlattice with nuclear (Fig. 2C) and magnetic (Fig. 2D) scattering length densities (SLDs). By examining numerous synthetic magnetic configurations, including the FM, sAFM, and spiral spin structures with varying ϕ, we confirmed that the structure shown in Fig. 2E indeed leads to a consistent in-plane simulation result of the experimental PNR spectra (Figs. S12-S15, Table S2, and Supplementary Text 2). While the exact rotation of the spin directions from one SRO layer to the other can be a subject of debate based on our experimental and fitting errors, it is evident that collinear spin configurations including FM and sAFM cannot account for the observed experimental results.

Both the non-collinear spiral spin state and its t_{STO}-dependent behavior reflect the existence of a nonconventional IEC in the SRO/STO superlattice. Several mechanisms can be considered to understand the magnetic interaction, including the dipole-dipole interaction, magnetic anisotropy, RKKY, orange peel interaction, coupling to the defect states, interlayer Dzyaloshinskii-Moriya interaction, and chiral phonon induced IEC (*2, 18, 34, 37-41*). First, the t_{STO}-dependent oscillatory behavior can rule out the dipole-dipole interaction and magnetic anisotropy, as they would only impose monotonic t_{STO}-dependence (*36*). Second, the RKKY cannot explain the interaction across the NM-I STO spacers (Fig. S16 and Supplementary Text 3) (*18, 38*). Third, Néel suggested that a sizeable roughness at heterointerfaces can lead to an IEC across NM-I spacers (*38*), yet our superlattices have a roughness in the order of an atomic unit cell (~0.4 nm) (Supplementary Fig. 3). Fourth, recent studies proposed that Schottky defects or metallic in-gap states can result in an IEC (*34, 37*), which is absent in our SRO/STO superlattices with suppressed charge transfer (See the Supplementary Text 4 for more detail) (*23, 24*). Fifth, interlayer Dzyaloshinskii-Moriya interaction can account for a non-collinear spiral spin state of synthetic magnetic layers. However, the Dzyaloshinskii-Moriya vector orientation should be defined along the in-plane direction of our experimental setup as was the case of other previously reported systems (*39, 40*), which is not consistent with the observed in-plane spiral spin structure.

Chiral phonon mediated IEC

The last candidate, *i.e.*, chiral phonon-spin coupling induced IEC is a plausible mechanism for elucidating the unconventional magnetic ground state, considering the facile formation and propagation of chiral phonons in the perovskite superlattices (*2, 13, 15, 41*). In particular, time-resolved optical spectroscopy has demonstrated that chiral phonons can dynamically mediate the long-range magnetic interaction across the NM-I spacer (*2*). They proposed a chiral phonon mediated-long-range spin exchange Hamiltonian, which explicates with the angular momentum transfer mechanism via chiral phonons and spin-orbit interaction, through the insulating layers. As the chiral nature of the phonon breaks the mirror symmetry, one can anticipate the existence of anti-symmetric IEC.

For the SRO/STO superlattices, strong spin-phonon and spin-orbit coupling of SRO lead to the creation of the chiral phonons (*20-22*). In particular, the ferromagnetic molecular field of SRO layers breaks the degeneracy, enabling a disparate population of the chiral phonons. The structural similarity of the perovskites and atomically sharp interfaces further facilitate the chiral phonon propagation, allowing chiral phonon-spin interaction in the neighboring SRO layers. Hence, we propose that spins in the FM layers can interact with each other through an NM-I spacer via chiral phonon-spin coupling, and the resultant unconventional magnetic ground state could be realized in the SRO/STO superlattices.

Chiral phonon-spin coupling evidenced by phonon Zeeman effect

The existence of chiral phonons and their coupling to spins in the SRO/STO superlattices was evidenced by *T*-dependent confocal Raman spectroscopy (see methods). Figure 3 shows a distinct split of a phonon mode at ~367 cm^{-1} into two modes at ~358 (phonon *A*) and ~386 cm^{-1} (phonon *B*) below T_c, in addition to the conventional phonon anomaly at T_c originating from the strong phonon-spin coupling in SRO (*20, 21*). Lattice dynamical calculation indicated that the modes correspond to oxygen vibrations with orthogonal polarizations in the orthorhombic bulk SRO (*20*). A superposition of the two orthogonal linear phonons with phase difference can create chiral phonons (insets of Fig. 3B) (*15*), which are to be distinguished from the chiral phonons in hexagonal lattices (*3*, *6*). The chiral phonon-spin coupling of SRO/STO superlattices was manifested by the phonon Zeeman splitting (*5*), which appeared without an external *H*-field. This reveals that the ferromagnetic molecular field in the SRO layer is strongly coupled to the chiral phonons (Fig. 3B). Whereas the two phonon modes are not degenerate in bulk SRO with orthorhombic structure, they should be degenerate in the thin film, with a tetragonal structural symmetry, as shown for the high *T* results. From the *T*-dependent behavior, we believe that the degeneracy lifting below T_c is related to the opposite energy shift of the chiral phonons with opposite chirality under the ferromagnetic molecular field. The relative splitting of phonon frequency ($\Delta\omega/\omega$) of SRO/STO superlattice is at ~0.076, which is the same magnitude in 4*f* rare-earth trihalides and Cd_3As_2 (*15*, *42-45*). This indicates the strong chiral phonon-spin coupling in SRO/STO superlattices. Although the population of phonon would decrease, the polarization of phonon can be enhanced with decreasing temperature, facilitating the magnetic interaction below T_c. In particular, the chiral phonon frequency (ω) is closely associated with the spatial spin rotation period (~3.6 nm) of the SRO/STO superlattices. Assuming the phonon velocity of SRO (v_s) to be ~2-6 nm ps^{-1} (*46*), the wavelength can be estimated as $2\pi v_s/\omega$ = ~1-3.6 nm for the chiral phonons showing the same order of magnitude to the periodicity of the synthetic magnetic oscillation. This correspondence suggests that chiral phonons created in the SRO layers can propagate across the NM-I STO spacers and induce IEC via chiral phonon-spin coupling.

Discussion

We have observed exotic spiral spin states with NM-I thickness-dependent oscillatory magnetic behavior, indicating the existence of IEC in atomically designed FM/NM-I heterostructures. The existence and the propagation of chiral phonons in the SRO/STO heterostructures led to the unconventional IEC via chiral phonon-spin coupling. Future theoretical studies are required to solidify the chiral phonon-mediated long-range magnetic ordering scenario in a static state. Nevertheless, the experimental observation itself provides a general intuition for understanding the emergent magnetic quantum phenomena, and the atomic-scale approach inspires the future combination of spintronics and phononics.

Materials and Methods

Superlattice growth

We chose the SRO and STO heterostructures since this system highly suppresses the charge transfer between SRO/STO interfaces, demonstrating intrinsic low-dimensional SRO layers (*23, 24*). We deliberately synthesized the $[\alpha|\beta]_\gamma$ superlattices, in which α-atomic unit cells layers of SRO and β-atomic unit cell layers of STO are systematically repeated for γ times along the growth direction, using pulsed laser epitaxy on (001) STO substrates. We controlled the number of atomic unit cells in the superlattices by employing a customized automatic laser pulse control system programmed using LabVIEW. The superlattice period (d_{SL}) was characterized by Bragg's law as $d_{SL} = \lambda/2$ $(\sin\theta_n - \sin\theta_{n-1})^{-1}$, where λ, n, and θ_n are the wavelength of the X-ray (0.154 nm for Cu K-α_1), the order of superlattice peaks, and the nth-order superlattice peak position, respectively. We deduced the thickness of SRO and STO layer utilizing XRR simulations, as shown in Fig. S2. We ablated stoichiometric ceramic targets using a KrF laser (248 nm, IPEX868, Lightmachinery) with a repetition rate of 5 Hz and a laser fluence of 1.5 J cm^{-2}. Both SRO and STO layers were deposited at 750 ºC and 100 mTorr of oxygen partial pressure for the stoichiometric condition of both materials. Note that atomically thin STO layers well-preserve their insulating behavior (Fig. S16).

Structural characterization

X-ray reflectivity and θ-2θ measurements were carried out by using high-resolution X-ray diffraction (HRXRD) of Rigaku Smartlab and PANalytical X'Pert X-Ray Diffractometer. We estimated the thickness of the superlattice period using Bragg's law as, $\Lambda = \frac{\lambda}{2}(\sin\theta_n - \sin\theta_{n-1})^{-1}$, where Λ, n, λ, and θ_n are the period thickness, superlattice peak order, X-ray wavelength, and nth-order superlattice peak position, respectively. All the superlattices exhibit a small thickness deviation, below 1 atomic unit cell (~0.4 nm), corresponding to the atomic step-size of the substrate. Atomic-scale imaging of SRO/STO heterostructure was performed on a spherical aberration-corrected scanning tunneling electron microscopy (STEM, ARM200CF, JEOL) working at 200 kV with high-angle annular dark-field (HAADF) imaging mode. The incident electron probe angle was ~23 mrad that translates to a probe size of ~0.78 Å. The angle range of the HAADF detector was 70–175 mrad. Cross-sectional thin samples for STEM observation were prepared by a dual-beam focused ion beam system (FIB, FEI Helios Nano Lab 450) and the following low-energy Ar ion milling at 700 V (Fischione Model 1040, Nanomill) was conducted for 15 min to eliminate damaged surface layers from heavy Ga ion beam milling in the FIB system.

Magnetization measurements

T- and *H*-dependence of magnetization behavior were measured using a Magnetic Property Measurement System (MPMS, Quantum Design). Field-cooled *M* (*T*) curves were obtained from 300 to 2 K with 0.01 T of *H*-field. The *M* (*H*) curves were obtained at 5, 50, and 85 K.

Polarized Neutron Reflectivity

PNR experiments were performed on the Magnetism Reflectometer at the Spallation Neutron Source at Oak Ridge National Laboratory (SNS, ORNL). The measurements were performed in closed-cycle refrigerator systems with an external H-field by using a Bruker electromagnet. We used highly polarized neutrons (polarization efficiency of 99 to 98.5 %) with wavelengths (λ) within a band of 2 to 8 Å. PNR spectra for two neutron polarizations (R^+ and R^-) were obtained by utilizing time-of-flight method, where a collimated polychromatic neutron beam impinges a sample at a grazing incidence angle (δ). The reflectivity signal was recorded as a function of wave vector transfer, $Q = 4\pi\sin(\delta)/\lambda$ (*47*). Nuclear and spin structures of superlattices were simulated by using GenX (*48*). To characterize the nuclear structure of the sample, we measured NR spectra at 300 K (Fig. S12A). Saturation magnetization values were estimated to 0.4 μ_B/Ru using PNR spectra at 85 K with 1 T (> coercive field at 85 K) of in-plane H-field (Fig. S12B), consistent with the result from MPMS. PNR is a depth-sensitive vector magnetometry method (*49*). In saturation, the layer magnetizations are fully magnetized parallel to the external field. In this case, only non-spin-flip reflectivity curves, R^{++} and R^{--} exist, which correspond to two orientations of neutron polarization. The reflectivity curves have well known characteristic features, like the oscillations determined by the total thickness and the Bragg peaks, corresponding to the periodicity of the superlattices. When the external magnetic field is released down to a small value of a guide field, the magnetizations in alternating SRO layers form a spiral structure, thus containing M_x and M_y components of magnetization. In this configuration the reflected signal will contain both non-spin-flip (R^{++} and R^{--}, determined by the parallel component of the magnetization vector M_y) and spin-flip (R^{+-} and R^{-+}, determined by the perpendicular component of the magnetization vector M_x) neutrons so that the resulting reflectivity curves will correspond to $R^+ = R^{++} + R^{+-}$ and $R^- = R^{--} + R^{-+}$. Our experiments were performed without spin-flip polarization analysis because the estimated experimental signal with spin-flip polarization is quietly small (Fig. S9). As it was demonstrated in ref. (*50*), without the full polarization analyses, the coupling angle between the magnetization vectors in the alternate magnetic layers can be effectively obtained through the data analyses by using the modulus of the magnetization vector obtained from the saturation and fitting only the alignment angles ϕ in the alternating SRO layers.

Confocal Raman spectroscopy

Raman spectra of SRO/STO superlattices were measured by utilizing a confocal micro-Raman (Horiba LabRam HR800) spectrometer using a HeNe laser with a wavelength of 632.8 nm (1.96 eV). To enhance the Raman cross-section of inelastic light scattering, we used the SRO/STO superlattice samples with 50 repetition number (*20*). We used a grating with 1800 grooves per mm and a focused beam spot size of ~5 µm. The power was maintained below ~0.3 mW to suppress any heating effects. With the backscattering geometry, we employed $z(xx)\bar{z}$ configuration to detect the A and B phonon modes, which are expected to exhibit a strong spin-phonon coupling. We note that an anomaly of phonon B at T_c represents the strong spin-phonon coupling in SRO/STO superlattices, consistent with previous SRO heterostructures (*20*, *21*). Lattice dynamical calculation suggested that the A and B phonon modes correspond to oxygen vibrations with orthogonal polarizations (A_g and B_{2g} modes, respectively) in the orthorhombic bulk SRO

(*20*). We also note that SRO has no structural phase transition below ferromagnetic transition temperatures (*21*). To obtain high-quality Raman spectra, we precisely adjusted the *z*-directional beam-position to achieve the optimal focus on the superlattice samples (*50*).

Junction transport measurement

The junction transport measurement was performed on the superlattice with atomically thin STO layers. Tunneling transport geometry was employed using Nb-doped (0.5 wt %) STO substrate as the bottom electrode and Au (~500 μm in diameter) as the top electrode. The top electrode was patterned on the surface of superlattices utilizing RF sputtering with a shadow mask. *T*-dependent tunneling resistance of superlattices was recorded using a physical property measurement system (PPMS**,** Quantum Design) with an excitation current of 0.3 μA.

References

1. R. Süsstrunk, S. D. Huber, Observation of phononic helical edge states in a mechanical topological insulator. *Science* **349**, 47 (2015).
2. V. L. Korenev *et al.*, Long-range *p–d* exchange interaction in a ferromagnet–semiconductor hybrid structure. *Nat. Phys.* **12**, 85-91 (2016).
3. L. Zhang, Q. Niu, Chiral Phonons at High-Symmetry Points in Monolayer Hexagonal Lattices. *Phys. Rev. Lett.* **115**, 115502 (2015).
4. T. F. Nova *et al.*, An effective magnetic field from optically driven phonons. *Nat. Phys.* **13**, 132-136 (2017).
5. D. Liu, J. Shi, Circular Phonon Dichroism in Weyl Semimetals. *Phys. Rev. Lett.* **119**, 075301 (2017).
6. H. Zhu *et al.*, Observation of chiral phonons. *Science* **359**, 579 (2018).
7. E. Thingstad, A. Kamra, A. Brataas, A. Sudbø, Chiral Phonon Transport Induced by Topological Magnons. *Phys. Rev. Lett.* **122**, 107201 (2019).
8. G. Grissonnanche *et al.*, Chiral phonons in the pseudogap phase of cuprates. *Nat. Phys.*, **16**, 1108 (2020).
9. X. Chen *et al.*, Entanglement of single-photons and chiral phonons in atomically thin WSe_2. *Nat. Phys.* **15**, 221-227 (2019).
10. L. Sheng, D. N. Sheng, & C. S. Ting, Theory of the Phonon Hall Effect in Paramagnetic Dielectrics. *Phys. Rev. Lett.* **96**, 155901 (2006).
11. L. Zhang & Q. Niu, Angular Momentum of Phonons and the Einstein–de Haas Effect. *Phys. Rev. Lett.* **112**, 085503 (2014).
12. D. A. Garanin & E. M. Chudnovsky, Angular momentum in spin-phonon processes. *Phys. Rev. B* **92**, 024421 (2015).
13. D. M. Juraschek, M. Fechner, A. V. Balatsky, N. A. Spaldin, Dynamical multiferroicity. *Phys. Rev. Mater.* **1**,014401 (2017).
14. C. Strohm, G. L. J. A. Rikken, and P. Wyder, Phenomenological Evidence for the Phonon Hall Effect. *Phys. Rev. Lett.* **95**, 155901 (2005).
15. D. M. Juraschek, N. A. Spaldin, Orbital magnetic moments of phonons. *Phys. Rev. Mater.* **3**, 064405 (2019).
16. X. Li, B. Fauqué, Z. Zhu, K. Behnia, Phonon Thermal Hall Effect in Strontium Titanate. *Phys. Rev. Lett.* **124**, 105901 (2020).

17. S. S. P. Parkin, Systematic variation of the strength and oscillation period of indirect magnetic exchange coupling through the 3*d*, 4*d*, and 5*d* transition metals. *Phys. Rev. Lett.* **67**, 3598 (1991).
18. P. Bruno, Theory of interlayer magnetic coupling. *Phys. Rev. B* **52**, 411 (1995).
19. B. Chen et al., All-oxide–based synthetic antiferromagnets exhibiting layer-resolved magnetization reversal. *Science* **357**, 191-194 (2017).
20. M. N. Iliev et al., Raman spectroscopy of $SrRuO_3$ near the paramagnetic-to-ferromagnetic phase transition. *Phys. Rev. B* **59**,364-368 (1999).
21. S. G. Jeong et al., Spin–phonon coupling in epitaxial $SrRuO_3$ heterostructures. *Nanoscale* **12**, 13926-13932 (2020).
22. J. M. Rondinelli, M. Stengel, N. A. Spaldin, Carrier-mediated magnetoelectricity in complex oxide heterostructures. *Nat. Nanotechnol.* **3**, 46-50 (2008).
23. Z. Zhong & P. Hansmann, Band Alignment and Charge Transfer in Complex Oxide Interfaces. *Phys. Rev. X* **7**,011023 (2017).
24. S. G. Jeong et al., Phase Instability amid Dimensional Crossover in Artificial Oxide Crystal. *Phys. Rev. Lett.* **124**, 026401 (2020).
25. S. G. Jeong et al., Propagation Control of Octahedral Tilt in $SrRuO_3$ via Artificial Heterostructuring. *Adv. Sci.* **7**, 2001643 (2020).
26. S. G. Jeong et al., Symmetry-Driven Spin-Wave Gap Modulation in Nanolayered $SrRuO_3$/$SrTiO_3$ Heterostructures: Implications for Spintronic Applications. *ACS Appl. Nano Mater.* **4**, 2160-2166 (2021).
27. S. W. Cho et al., Tailoring topological Hall effect in $SrRuO_3$/$SrTiO_3$ superlattices. *Acta. Mater.* **216**, 117153 (2021).
28. R. Masuda, Y. Kaneko, Y. Tokura, and Y. Takahashi, Electric field control of natural optical activity in a multiferroic helimagnet. *Science.* **372**, 6541 (2021).
29. T. Yokouchi, F. Kagawa, M. Hirschberger, Y. Otani, N. Nagaosa & Y. Tokura, Emergent electromagnetic induction in a helical-spin magnet. *Nature.* **586**, 232-236 (2020).
30. S. Jiang, H. Xie, J. Shan, K. F. Mak, Exchange magnetostriction in two-dimensional antiferromagnets. *Nat. Mater.* **19**, 1295-1299 (2020).
31. C. L. Platt et al., Magnetic interlayer coupling in ferromagnet/insulator/ferromagnet structures. *Phys. Rev. B* **61**, 9633 (2000).
32. S. J. Zhu et al., Oscillatory exchange coupling in $La_{0.67}Sr_{0.33}MnO_3$/$SrTiO_3$ superlattices. *Appl. Phys. Lett.* **91**, 012505 (2007).
33. L. E. Nistor et al., Oscillatory interlayer exchange coupling in MgO tunnel junctions with perpendicular magnetic anisotropy. *Phys. Rev. B* **81**, 220407(R) (2010).
34. W. M. Lü et al., Long-range magnetic coupling across a polar insulating layer. *Nat. Commun.* **7**, 11015 (2016).
35. S. Thota, S. Ghosh, S. Nayak, D. C. Joshi, P. Pramanik, K. Roychowdhury, and S. Das, Finite-size scaling and exchange-bias in $SrRuO_3$/$LaNiO_3$/$SrRuO_3$ trilayers. *J. Appl. Phys.* **122**, 124304 (2017).36. M. R. Fitzsimmons & C. F. Majkrzak, *Modern Techniques for Characterizing Magnetic Materials.* (Kluwer, 2005). 37. J. D. Hoffman et al., Oscillatory Noncollinear Magnetism Induced by Interfacial Charge Transfer in Superlattices Composed of Metallic Oxides. *Phys. Rev. X* **6**, 041038 (2016).
38. J. M. D. Coey, *Magnetism and Magnetic Materials*. (Cambridge University Press, Cambridge, 2010).

39. A. Fernández-Pacheco et al., Symmetry-breaking interlayer Dzyaloshinskii–Moriya interactions in synthetic antiferromagnets. *Nat. Mater.* **18**, 679-684 (2019).
40. D.-S. Han et al., Long-range chiral exchange interaction in synthetic antiferromagnets. *Nat. Mater.* **18**, 703-708 (2019).
41. M. Bombeck et al., Magnetization precession induced by quasitransverse picosecond strain pulses in (311) ferromagnetic (Ga,Mn)As. *Phys. Rev. B* **87**, 060302 (2013).
42. G. Schaack, Observation of circularly polarized phonon states in an external magnetic field. *J. Phys. C: Solid State Phys.* **9**, 297 (1976).
43. P. Thalmeier & P. Fulde, Optical phonons of Rare-Earth halides in a magnetic field. *Z. Phys.* **26**, 323-328 (1977).
44. D. M. Juraschek, T. Neuman, and P. Narang, https://arxiv.org/abs/2007.10556 (2020).
45. B. Cheng et al., A Large Effective Phonon Magnetic Moment in a Dirac Semimetal. *Nano. Lett.* **20**, 5991 (2020).
46. Š. Masys, V. Jonauskas, A first-principles study of structural and elastic properties of bulk $SrRuO_3$. *J. Chem. Phys.* **139**, 224705 (2013).
47. V. Lauter, H. Ambaye, R. Goyette, W.-T. H. Lee, A. Parizzi, A. Highlights from the magnetism reflectometer at the SNS. *Physica B Condens. Matter* **404**, 2543-2546 (2009).
48. M. Bjorck, G. Andersson, GenX: an extensible X-ray reflectivity refinement program utilizing differential evolution. *J. Appl. Crystallogr.* **40**, 1174-1178 (2007).
49. V. Lauter-Pasyuk, Neutron grazing incidence techniques for nano-science. *Soc. Fr. Neutron.* **7**, s221-s240 (2007).
50. V. Lauter-Pasyuk et al., Magnetic neutron off-specular scattering for the direct determination of the coupling angle in exchange-coupled multilayers. *J. Magn. Magn.* **226-230**, 1694-1696 (2001).
51. A. Seo et al., Compressive strain induced enhancement of exchange interaction and short-range magnetic order in Sr_2IrO_4 investigated by Raman spectroscopy. *Phys. Rev. B* **100**, 165106 (2019).
52. D. Kim et al., Mean-field behavior with Gaussian fluctuations at the ferromagnetic phase transition of $SrRuO_3$. *Phys. Rev. B* **67**, 100406(R) (2003).
53. S. J. Blundell, M. Gester, J. A. C. Bland, H. J. Lauter, V. V. Pasyuk, and A. V. Petrenko, Spin-orientation dependence in neutron reflection from a single magnetic film. *Phys. Rev. B.* **51**, 9395(R) (1995).
54. H. N. Lee, S. S. Ambrose Seo, W. S. Choi, C. M. Rouleau, Growth control of oxygen stoichiometry in homoepitaxial $SrTiO_3$ films by pulsed laser epitaxy in high vacuum. *Sci. Rep.* **6**, 19941 (2016).

Acknowledgments

This research used resources at the Spallation Neutron Source, a DOE Office of Science User Facility operated by the Oak Ridge National Laboratory. We thank TSP. and JK for technical support of junction transports and KTK and SW for valuable discussions. We also thank Core Research Facilities, Pusan National University for MPMS.

Funding: Include all funding sources, including grant numbers, complete funding agency names, and recipient's initials. Each funding source should be listed in a separate paragraph such as:
National Research Foundation of Korea NRF-2021R1A2C2011340 (SGJ, WSC)

National Research Foundation of Korea NRF-2020K1A3A7A09077715 (SGJ, JK, SP, WSC)
National Research Foundation of Korea NRF-2020K1A3A7A09077715 (YMK)
National Science Foundation (DMR-1454200) (AS)
Alexander von Humboldt Foundation (Research Fellowship for Experienced Researchers) (AS)

Author contributions:

Conceptualization: SGJ, WSC
Methodology: SGJ, JK, AS, SP, HYJ, YMK, VL, WSC
Data curation: SGJ, JK, AS, SP, YMK, VL
Investigation: SGJ, SP, VL, WSC
Validation: AS, SP, VL, TE, JHH, WSC
Visualization: SGJ, WSC
Supervision: WSC
Project administration: WSC
Funding acquisition.: WSC
Writing—original draft: SGJ, WSC
Writing—review & editing: SGJ, AS, SP, VL, JHH, WSC

Competing interests: : Authors declare no competing interests.

Data and materials availability: All data for samples and reference materials are available in the supplementary materials.

Figures and Tables

Table 1. The chiral phonon induced emergent spin states.

Phenomena	Systems	References
Phononic helical edge state	Mechanical topological insulator	(*1*)
AC Stark effect	CdTe quantum well	(*2*)
Phonon Hall effect	Honeycomb lattice, cuprates, paramagneticdielectrics	(*10, 14, 16*)
Optically driven effective magnetic field	$ErFeO_3$ (Perovskite)	(*4*)
Topologically-induced viscosity split	Weyl Semimetals	(*5*)
Intervalley transfer of phonon angular momentum	WSe_2 (Honeycomb lattice)	(*6*)
Topological magnon-phonon coupling	Honeycomb lattices	(*7*)
Pseudogap phase of superconductor	Cuprates	(*8*)
Einstein–de Haas Effect	Honeycomb, Kagome, triangle, and square lattices	(*3*, *11, 12*)
Dynamic multiferroicity	Perovskites	(*6*)
Resonant magnon excitation	$ErFeO_3$ (Perovskite)	(*13, 15*)
Dzyaloshinskii-Moriya-type electromagnon	$TbMnO_3$ (Perovskite)	
Inverse Faraday effect	$DyFeO_3$ (Perovskite)	
Phonon Zeeman effect	Binary compounds, perovskites, transition metal dichalcogenides	
Entanglement of single-photon and phonon	WSe_2 (Honeycomb lattice)	(*9*)
Static interlayer exchange coupling	$SrRuO_3/SrTiO_3$ superlattice	Current study

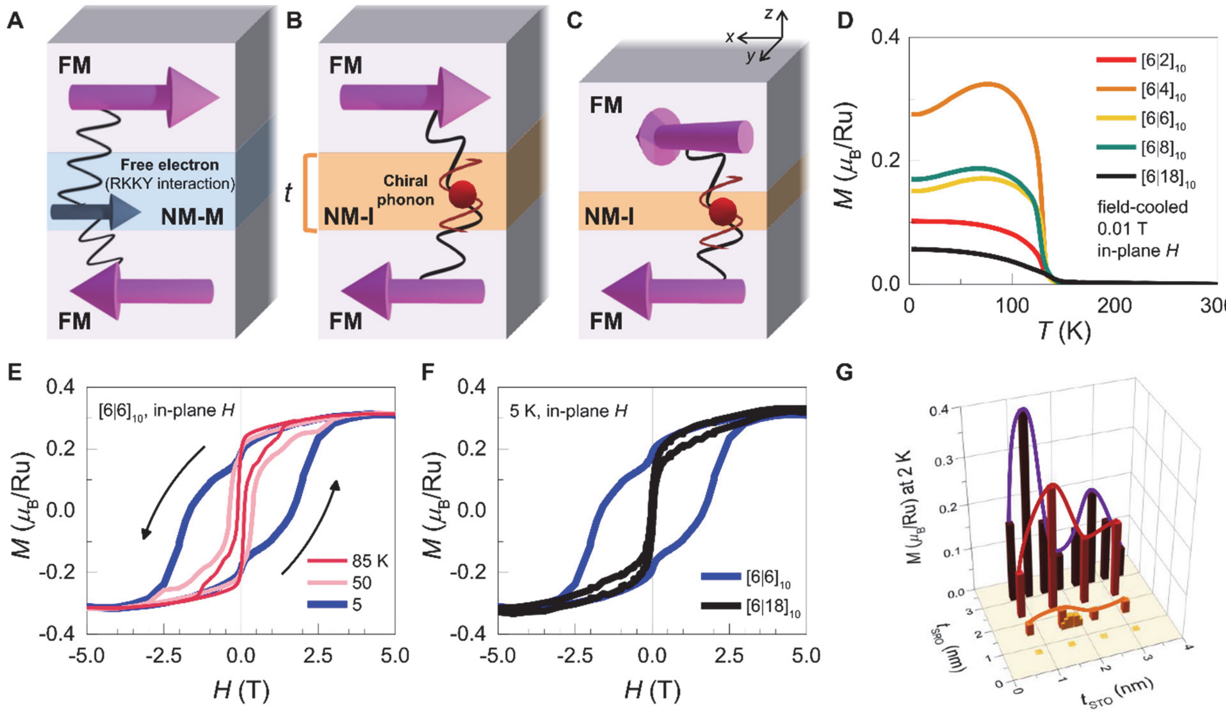

Fig. 1. Chiral phonon-mediated IEC and resultant t_{STO}-dependent magnetic behavior of SRO/STO superlattices. Schematic diagrams of IEC across (A) an NM-M spacer via free-electron mediated RKKY interaction and (B and C) NM-I spacers via chiral phonon-mediated interaction with different *t*. (D) In-plane *M* (*T*) curves of SRO/STO superlattices with systematically changing t_{STO}. T^* is marked with an arrow. (E) *M* (*H*) curves of the superlattices at 85, 50, and 5 K. The arrows indicate the directions of the *H*-field. (F) *M* (*H*) curves of the superlattices with different t_{STO}. The curves are measured at 5 K. (G) Oscillatory magnetic behavior of the *M* value as a function of t_{STO}. The values were obtained at 2 K with 0.01 T of in-plane *H*-field. The solid lines are the guide to the eye.

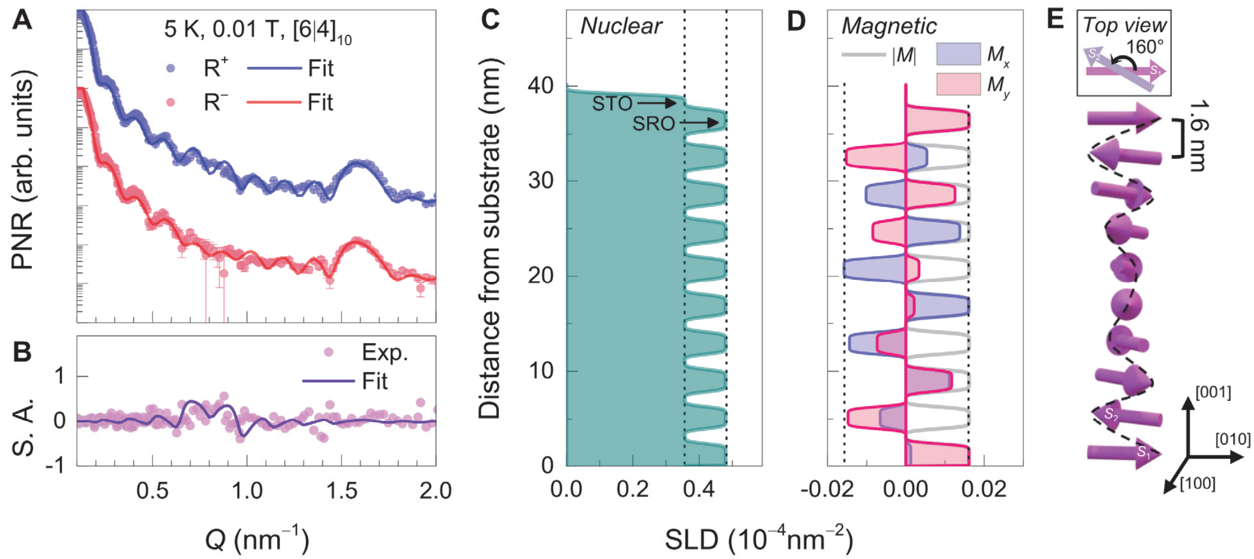

Fig. 2. Non-collinear spiral spin state of the SRO/STO superlattice. (A) PNR spectra for the spin-up (R^+) and spin-down (R^-) polarized neutrons and (B) S. A. for [6|4] superlattice at 5 K. The measurement was performed with 0.01 T of in-plane *H*-field. The symbols and solid lines indicate experimental data and fit using the model in (C-E), respectively. The error bars represent one standard deviation. (C) Nuclear SLD depth profile of the superlattice. (D) Magnetic SLD depth profile with *x*- and *y*-directional *M* values (M_x and M_y). Gray solid line is the absolute value of the total magnetic SLD for each SRO layer within the superlattice (~0.4 μ_B/Ru). The vertical dashed lines in (C) and (D) are guides to the eye. (E) Schematic diagram of the spin configuration in the SRO/STO superlattice. The top view displays the ϕ = 160º between the magnetization directions (S_1 and S_2) in the two neighboring SRO layers when t_{SRO} = 1.6 nm. External *H*-field has been applied along the [010] direction (*y*).

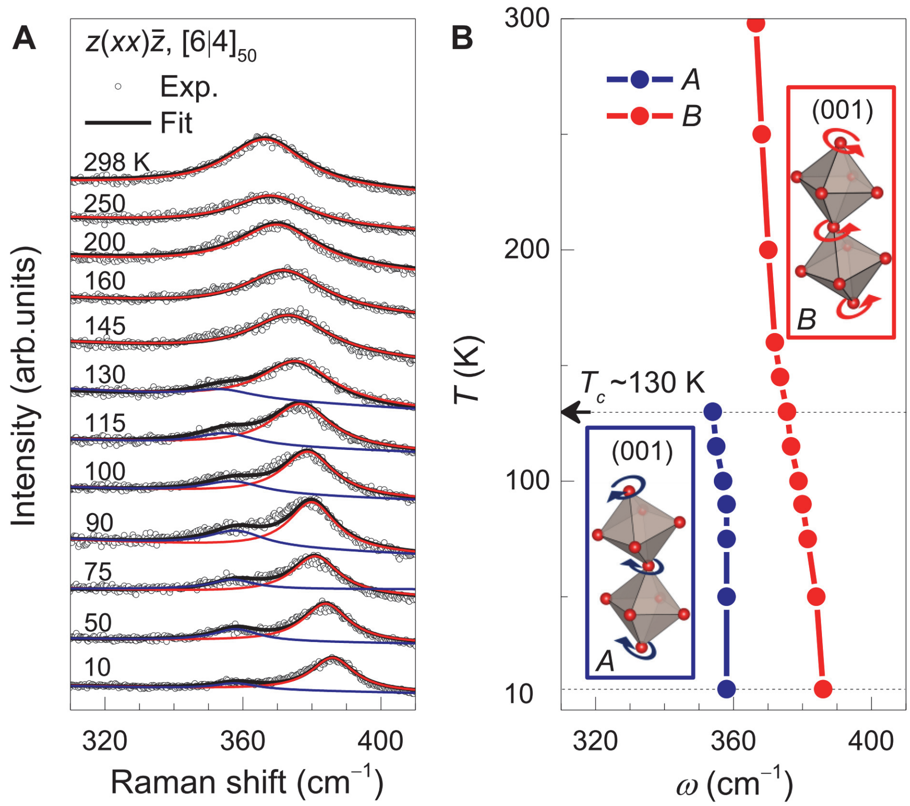

Fig. 3. Chiral symmetry breaking in SRO/STO superlattices. (A) T-dependent confocal Raman spectra in $z(xx)\bar{z}$ polarization of a [6|4] superlattice (The results of a [6|8] superlattices are in Fig. S17) . The symbols and solid lines represent experimental data and fit for the Raman spectra, respectively. Blue and red solid lines correspond to the A and B phonons, respectively, as described in the insets of (B). (B) T-dependent ω splitting below T_c. The insets schematically represent the expected chiral phonon modes of SRO. The dotted horizontal lines indicate (up) T_c of SRO and (down) the lowest T (10 K) of the measurement.

Supplementary Materials

Supplementary Text 1 to 4

Figs. S1 to S17

Tables S1 to S2

References (*52* to *54*)